

# Antisite Defects and Chemical Expansion in Low-damping, High-magnetization Yttrium Iron Garnet Films

Jose Santiso,<sup>[a]</sup> Carlos García,<sup>[b]</sup> Cristian Romanque,<sup>[b]</sup> Loïc Henry,<sup>[c]</sup> Nicolas Bernier,<sup>[c]</sup> Núria Bagués,<sup>[d]</sup> José Manuel Caicedo,<sup>[a]</sup> Manuel Valvidares,<sup>[e]</sup> and Felip Sandiumenge<sup>\*,[f]</sup>

**Abstract:** Yttrium iron garnet is widely investigated for its suitability in applications ranging from magneto-optical and microwave devices to magnonics. However, in the few-nanometer thickness range, epitaxial films exhibit a strong variability in magnetic behavior that hinders their implementation in technological devices. Here, direct visualization and spectroscopy of the atomic structure of a nominally stoichiometric thin film, exhibiting a small damping factor of  $3.0 \cdot 10^{-4}$ , reveals the occurrence of Y-excess octahedral antisite defects. The two-magnon strength is very small,  $\Gamma_0$

$\approx 10^{-6}$  Oe, indicating a very low occurrence of scattering centers. Notably, the saturation magnetization,  $4\pi M_s = 2.10 (\pm 0.01)$  kOe, is higher than the bulk value, in consistency with the suppression of magnetic moment in the minority octahedral sublattice by the observed antisite defects. Analysis of elemental concentration profiles across the substrate-film interface suggests that the Y-excess is originated from unbalanced cationic interdiffusion during the early growth stages.

## Introduction

Magnetic garnets combine infrared optical transparency, a prominent Faraday effect, insulating behavior, very small spin-wave damping factors, and low dielectric losses,<sup>[1]</sup> which make them highly attractive in magneto-optical and microwave applications.<sup>[2,3]</sup> Among these materials yttrium iron garnet (YIG), a ferrimagnetic insulator exhibiting an extremely low intrinsic Gilbert damping parameter of  $\alpha \approx 3 \cdot 10^{-5}$ , appears as an ideal material for the emerging field of magnonics.<sup>[4–6]</sup> For

the latter applications, downscaling is a prerequisite which so far complicates control on magnetic properties due to their strong sensitivity to film strain and composition, and demands a thorough understanding of the growth mechanism. Traditionally, YIG films have been grown by liquid phase epitaxy, offering excellent epitaxial quality and bulk-like properties.<sup>[7–9]</sup> Although films grown by this technique typically have thicknesses comprised in the micrometer to millimeter range, low-damping films below 40 nm have been reported.<sup>[10]</sup> Nonetheless, advances in oxide thin film deposition have allowed the growth of high quality thin films, well below 40 nm, by a number of techniques including sputtering,<sup>[11,12]</sup> pulsed laser deposition (PLD),<sup>[13–16]</sup> and chemical solution deposition.<sup>[17]</sup> Although damping values as small as  $7 \cdot 10^{-5}$  have been obtained by PLD,<sup>[15]</sup> compared with liquid phase epitaxial thick films, thin films still exhibit a strong variability in the magnetic properties. For instance, unusually high magnetic anisotropy has been reported in PLD films,<sup>[13,14]</sup> or both magnetization suppression<sup>[11]</sup> and exceptionally high magnetization<sup>[12]</sup> have been reported in sputtered samples.

The commonly used substrate for YIG is  $\text{Gd}_3\text{Ga}_5\text{O}_{12}$  (GGG) in (111) orientation, which provides a very small tensile misfit strain of 0.06%, allowing films to grow coherently in the absence of misfit dislocations. Thus, in the absence of a significant misfit, the scatter of physical behavior observed in thin films is to be sought on interdiffusion and defect chemistry rather than strain effects. In this sense, it has been argued that  $\text{Fe}^{3+}$  vacancies cause the unusual magnetic anisotropy,<sup>[13,14]</sup> or that magnetization suppression in sputtered films results from an enrichment in  $\text{Gd}^{3+}$  ions,<sup>[11]</sup> while other studies point to a preferential  $\text{Ga}^{3+}$  diffusion into the film causing a dead layer.<sup>[16]</sup> Besides interdiffusion among equivalent sublattices, YIG films often exhibit an anomalous lattice stretching along the growth direction<sup>[18–20]</sup> and rhombohedral distortions,<sup>[19,20]</sup> which very likely reflect chemical expansion effects caused by point

[a] Dr. J. Santiso, Dr. J. M. Caicedo  
Catalan Institute of Nanoscience and Nanotechnology (ICN2)  
CSIC and the Barcelona Institute of Science and Technology (BIST)  
Campus de la UAB, 08193 Bellaterra, Catalonia (Spain)

[b] Dr. C. García, Dr. C. Romanque  
Departamento de Física y Centro Científico Tecnológico de Valparaíso –  
CCTVal Universidad Técnica Federico Santa María  
Av. España 1680, 2390123, Valparaíso (Chile)


[c] Dr. L. Henry, Dr. N. Bernier  
Université Grenoble Alpes  
CEA, LETI  
F-38000 Grenoble (France)

[d] Dr. N. Bagués  
Center for Electron Microscopy and Analysis  
The Ohio State University  
43212 Columbus, Ohio (USA)

[e] Dr. M. Valvidares  
ALBA Synchrotron Light Source  
08290 Cerdanyola del Vallès, Catalonia (Spain)

[f] Dr. F. Sandiumenge  
Institut de Ciència de Materials de Barcelona (ICMAB-CSIC)  
Campus de la UAB, 08193 Bellaterra, Catalonia (Spain)  
E-mail: felip@icmab.cat

 Supporting information for this article is available on the WWW under <https://doi.org/10.1002/cnma.202200495>

 © 2022 The Authors. ChemNanoMat published by Wiley-VCH GmbH. This is an open access article under the terms of the Creative Commons Attribution Non-Commercial NoDerivs License, which permits use and distribution in any medium, provided the original work is properly cited, the use is non-commercial and no modifications or adaptations are made.

defects, particularly antisite. Altogether, these observations suggest a complex interplay between interdiffusion, defect chemistry and growth conditions, that remains poorly understood.

The general formula of YIG is  $Y^{(c)}_3Fe^{(a)}_2Fe^{(d)}_3O_{12}$  ( $la3d$ ), where letters (c), (a), (d) are Wyckoff sites here denoting dodecahedral, octahedral and tetrahedral coordination, respectively.<sup>[21]</sup> Atomistic calculations show a strong tendency for point defect formation, with oxygen and iron vacancies, and antisite defects (excess Y sitting at octahedral sites,  $Y^{(a)}$ ), exhibiting the lowest formation energies.<sup>[22,23]</sup> Antisite defects can also be of disorder type, formed by the exchange between (c) and (a)-site cations according to the disorder reaction  $Y^{(c)} + Fe^{(a)} \rightarrow Y^{(a)} + Fe^{(c)}$ , keeping the nominal stoichiometry unaltered. The energy of this reaction is 0.8 eV per defect,<sup>[24]</sup> which is comparatively low enough to favor the occurrence of  $Y^{(a)}$  antisites in stoichiometric crystals as native defects, in agreement with nuclear magnetic resonance spectroscopy studies.<sup>[25–27]</sup> Given that YIG ferrimagnetism arises from the unbalanced antiferromagnetic coupling between 16 octahedral and 24 tetrahedral sites hosting the  $Fe^{3+}$  ions, magnetic dilution by Y antisites or Fe vacancies in the different sublattices may either increase or suppress net magnetic moment.<sup>[23,28,29]</sup> Note, however, that since (a) and (c) sites have parallel spin coupling,<sup>[30]</sup> disorder-type antisites alone leave the net moment unaltered.

In this work we use aberration-corrected scanning transmission electron microscopy (STEM) imaging and spectroscopy, to elucidate the formation mechanism and spatial distribution of point defects. We show that local off-stoichiometry resulting from unbalanced cationic interdiffusion profiles across the substrate-film interface leads to the accumulation of excess-type antisite defects within the interdiffusion zone and a background defect concentration throughout the film volume. Despite this chemical complexity, ferromagnetic resonance (FMR) measurements yield a small Gilbert damping of  $3.0 \cdot 10^{-4}$ , comparable with best values obtained by PLD,<sup>[15]</sup> and an almost negligible two-magnon scattering (TMS) strength parameter of  $\Gamma_0 = 10^{-6}$  Oe, indicating magnetic homogeneity. The saturation magnetization determined from FMR,  $4\pi M_s = 2.10 (\pm 0.01)$  kOe, is higher than the bulk value: 1.73–1.75 kOe,<sup>[31]</sup> which is attributed to the suppression of magnetic moment in the minority octahedral sublattice by non-magnetic  $Y^{(a)}$  antisites.

## Results and Discussion

Figure 1a shows a high resolution XRD scan around the 444 reflection of both film and substrate. From the film peak position an interplanar spacing along the film normal of  $d_{444} = 1.8075 \text{ \AA}$  is obtained, which indicates an anomalous lattice stretching of 1.10% relative to the bulk value,  $d_{444} = 1.78776 \text{ \AA}$  ( $a = 12.376 \text{ \AA}$ ).<sup>[21]</sup> The XRD fringes indicate a high crystal coherence of the film and the period of the oscillations corresponds to a film thickness of 25 nm, in good agreement with STEM observations. XRD reciprocal space mapping around the asymmetric 880 YIG reflection indicates perfect in-plane matching with the substrate (see Figure 1b), and a reduced

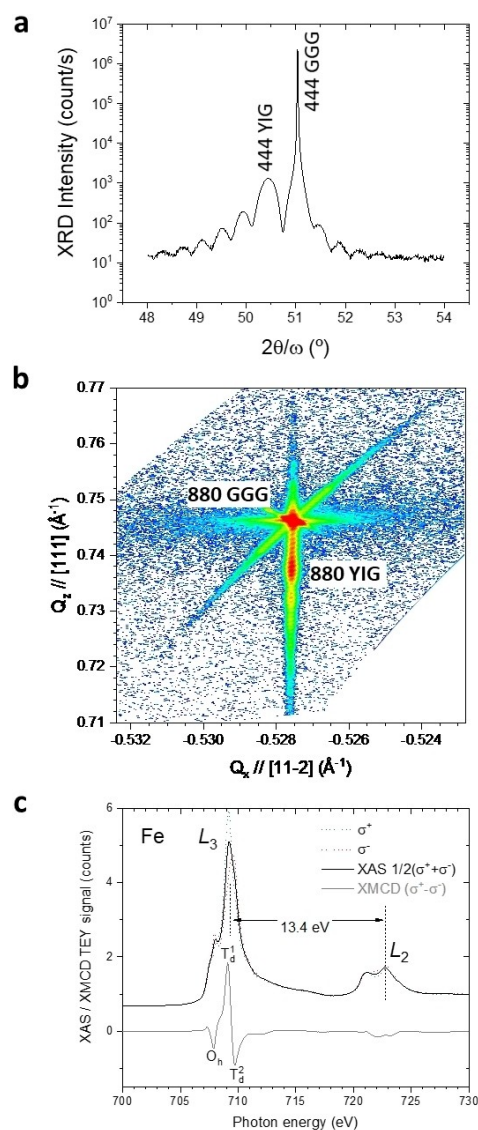


**Figure 1.** a) High resolution  $2\theta/\omega$  scans about the 444 reflection of GGG and YIG. Fringes indicate a high crystal coherence and a film thickness of 25 nm. b) Reciprocal space map around the 880 reflection. Vertical alignment of the GGG and YIG reflections indicates perfect in-plane matching. c) Fe- $L_{2,3}$  XAS and XMCD spectra acquired under an applied field of 2T. The measured energy difference  $E(L_2) - E(L_3) = 13.4 \text{ eV}$  indicates trivalent iron (see Supplemental Information S1), and main spectral features:  $O_h$ ,  $T_d$  and  $T_d'$ , are consistent with the expected YIG magnetic structure.

cubic interaxial angle of  $89.38^\circ$ , in consistency with a rhombohedral distortion resulting from the stretching along the cubic body diagonal. By analyzing the Fe- $L_{2,3}$  edge XAS signal (Figure 1c) we find that Fe ions are in a trivalent state, at least within the first 2–5 nm beneath the film surface sampled by the X-rays (see Supplemental Information S1 and references therein). Figure 1c also shows the corresponding XMCD spectrum obtained under a magnetic field of 2 T. The main features are a prominent positive maximum at 709.1 eV bounded by two negative minima at 707.9 eV and 709.7 eV, which can be assigned to the octahedral ( $O_h$ ) and tetrahedral ( $T_d$ ) sublattices,

confirming the expected YIG magnetic structure and the trivalent state of Fe ions.

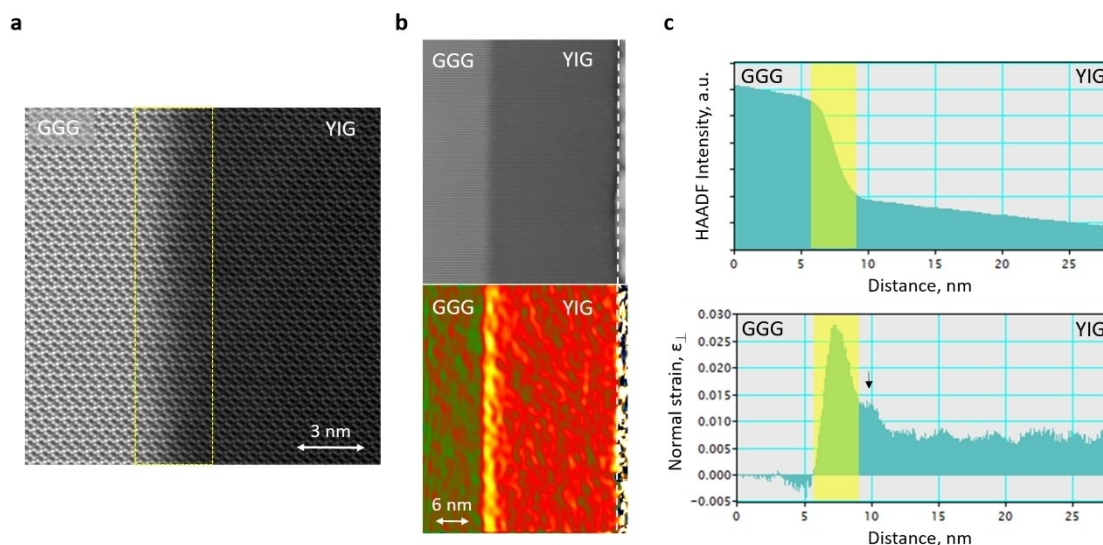
Similar distortions, with stretching values comprised between 1.0 and 1.5%, and rhombohedral angles of about  $89.5^\circ$ , have been observed by several authors.<sup>[18–20]</sup> In fact, from reported diffraction data one observes that this phenomenon is more common than manifested in the literature. For instance, normal strains ranging from 0.42% to 0.11% are observed in films with thicknesses comprised between 16 nm and 164 nm,<sup>[12]</sup> and a value of 0.96% is inferred from data corresponding to a 250 nm thick film in ref. [11] Interestingly, these distortions are markedly enhanced up to 2.7% (stretching) and  $88.8\text{--}89.1^\circ$  (rhombohedrality) in Y-excess films exhibiting a high concentration of  $Y^{(a)}$  antisites.<sup>[23]</sup> While in those off-stoichiometric films such large distortions can be explained by the ionic radii difference between  $Fe^{3+}$  and  $Y^{3+}$  ions in octahedral coordination, 0.645 Å and 0.900 Å, respectively,<sup>[32]</sup> in nominally stoichiometric films the origin of the observed distortion remains unclear.

Figure 2a shows a cross-section high resolution annular dark-field (HAADF) image viewed along the  $[01\bar{1}]$  zone axis. Since this is an incoherent image with contrast proportional to  $Z^{1.7}$  ( $Z$  is the atomic number),<sup>[33]</sup> the GGG substrate appears brighter than the YIG film. In agreement with the XRD data, the image shows perfect lattice continuity across the interface. It can be observed, however, that the transition from the substrate to the film is not abrupt, but exhibits an apparent width of about 4 nm (area framed with dashed line), significantly larger than the rms roughness of the substrate surface, suggesting a chemically diffuse interface.

Figure 2b shows a mapping of the normal strain ( $\epsilon_{\perp}$ ) over the corresponding image shown in the upper panel, derived

from geometrical phase analysis (GPA,<sup>[34]</sup>). A striking feature is the layer of high (yellow) contrast adjacent to the interface, which manifests as a prominent peak in the strain profile depicted in Figure 2c (bottom panel). The corresponding HAADF contrast profile is depicted in Figure 2c (upper panel). We note that due to the large difference between the Gd ( $Z = 64$ ) and Y (39), Ga (31) and Fe (26) atomic numbers, the apparent width of the contrast transition region can be considered to mostly reflect the interdiffusion length of  $Gd^{3+}$  ions. Comparing the contrast and strain profiles one observes that the thickness of the stretched layer is similar to that of the substrate to film transition region, both indicated by yellow shadowings. Remarkably, beyond this feature, instead of recovering the bulk lattice dimensions, the film still retains an oscillating positive background strain. The average strain value within the homogeneous region is  $\langle \epsilon_{\perp} \rangle = 0.007$  with a standard deviation  $\sigma = 0.003$ . Including the interfacial region yields  $\langle \epsilon_{\perp} \rangle = 0.010$ , similar to the averaged value derived from XRD results, 0.011.

We used EELS at the Fe- $L_{2,3}$  edge and EDS mapping to determine the spatial homogeneity of the oxidation state of Fe and the elemental distribution over the windows marked in Figure 3a. The EEL spectra, depicted in Figure 3b, were analyzed using three components:  $L_3$ ,  $L_2$ , and a third one, labelled \*, to account for the low intensity shoulder on the high energy side of the  $L_3$  peak, as illustrated in the inset, and results are depicted in Figure 3c. The  $L_3$  peak is located at 709.2 eV in good agreement with XAS and, with the exception of the outermost spectrum (distance = 25 nm), neither its position nor the energy difference relative to the  $L_2$  signal do change through the thickness of the film, thus indicating a homogeneous trivalent state of Fe ions. Under the assumption of cation stoichiometry,



**Figure 2.** a) Cross-section HAADF image of the GGG/YIG interface viewed along the  $[01\bar{1}]$  direction. The framed region shows a contrast transition region consistent with a chemically diffuse interface. b) GPA mapping of the normal strain component ( $\epsilon_{\perp}$ ) over the image shown in the upper panel, comprising the whole film thickness. The film surface is indicated by a dashed line. c) Upper panel: HAADF intensity profile integrated over the image shown in b). Lower panel: Normal strain profile integrated over the GPA map shown in b). Yellow shadowings emphasize the correspondence between the widths of the contrast transition region marked in a) and the highly strained interfacial layer. The arrowed peak corresponds to a strain maximum out of the Gd diffusion length (see text).

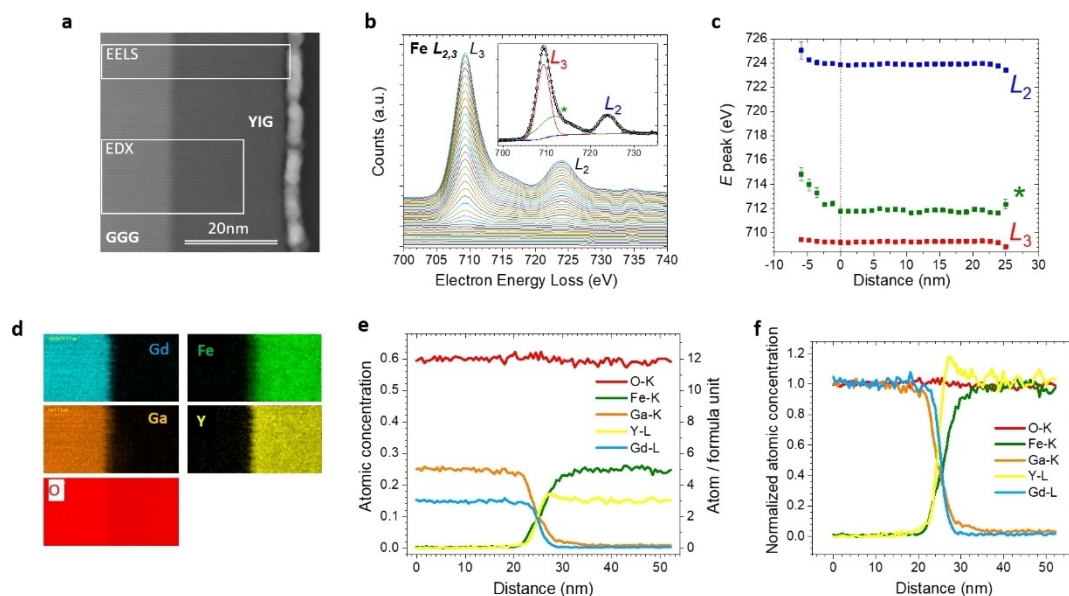


**Figure 3.** a) Cross section HAADF image illustrating the areas used for EELS and EDS analyses. b) Through thickness sequence of EEL spectra obtained from the corresponding area marked in a). The inset illustrates the fitting procedure employed to analyze the spectra. c) Position dependence along the film normal of the energies corresponding the  $L_3$ ,  $L_2$  and \* spectral features. A dashed line marks the position of the interface. d) EDS elemental maps acquired from the corresponding area marked in a). e) Elemental concentration profiles across the substrate-film interface as determined from integration over the corresponding maps shown in d). f) Normalized elemental concentration profiles.

this result is consistent with the absence of oxygen vacancies. However, we cannot rule out their presence as they could also form to compensate for cation vacancies.

As shown in Figure 3d, EDS results indicate a homogeneous cation distribution within the film and signal blurring in the vicinity of the interface, consistent with the contrast transition zone observed in HAADF images. Corresponding concentration profiles, shown in Figure 3e, indicate that larger ions,  $Gd^{3+}$  and  $Y^{3+}$ , exhibit smaller diffusion lengths,  $\approx 4$  nm, than  $Ga^{3+}$  and  $Fe^{3+}$ ,  $\approx 8.5$  nm. Values of interdiffusion lengths reported in the literature for this system are controversial. Liu et al. report HAADF images with a sharp contrast change between the GGG substrate and the YIG film, and EDS elemental profiles exhibiting chemical intermixing over 2.3 nm which they attribute to delocalization of the X-ray emission signal.<sup>[35]</sup> Gallagher et al. report HAADF images with a smoother contrast transition and chemical intermixing over 4 nm, as determined by EDS, which also attribute to delocalization effects.<sup>[12]</sup> On the other hand, Mitra et al. observe a smooth transition region in HAADF images and a 6 nm wide intermixing region, as determined by EELS, which they consider representative of true interdiffusion effects.<sup>[11]</sup> In the present case, the differential behavior exhibited by the different elements, together with the HAADF contrast transition between the substrate and the film, strongly support the interpretation of our EDS results in terms of true chemical intermixing.

In order to compare in more detail the behavior of the different ions, Figure 3f shows the diffusion profiles normalized to the nominal cation stoichiometry, i.e. the rate of occupation of dodecahedral sites by Gd and Y, and of the sum of octahedral and tetrahedral sites by Ga and Fe. Two features are

particularly relevant to the defect chemistry of the interfacial region. The first one concerns the marked asymmetry between the diffusion behavior of Fe/Y and Ga/Gd ions. While from the substrate side Gd and Ga draw rather similar profiles, from the film side the Y profile is much steeper than the Fe one and clearly reveals an excess peak  $\sim 20$  at% above the stoichiometric level. Moreover, the Y profile shows fluctuations above the stoichiometric level throughout the bulk film. The differential behavior between Y and Fe ions in fact suggests that the formers are replacing iron at octahedral or tetrahedral sites forming antisite defects. Recalling that the HAADF intensity profile shown in Figure 2 is dominated by the Gd atomic number, it can be inferred that the position of the Y-excess layer coincides with the position of the (arrowed) shoulder adjacent to the main peak in the strain profile, which lies out of the contrast transition region. Hence, these observations allow to associate the main strain peak with the Gd interdiffusion region and its shoulder with the position of an adjacent Y-excess layer. Thus, these strain peaks would be consistent with the chemical expansion expected for the occurrence of Gd and Y antisite defects.

The location of the Y-enriched layer at the boundary of the Gd diffusion length strongly suggests a dominant role of Gd ions diffusing from the substrate during the early stages of nucleation and growth. The partial occupancy of dodecahedral (c) sites by Gd may cause an accumulation and displacement of Y ions on the surface of the growing film that would eventually cease when its thickness reaches the Gd diffusion length, leading to the observed Y peak immediately ahead of the reach of Gd ions.

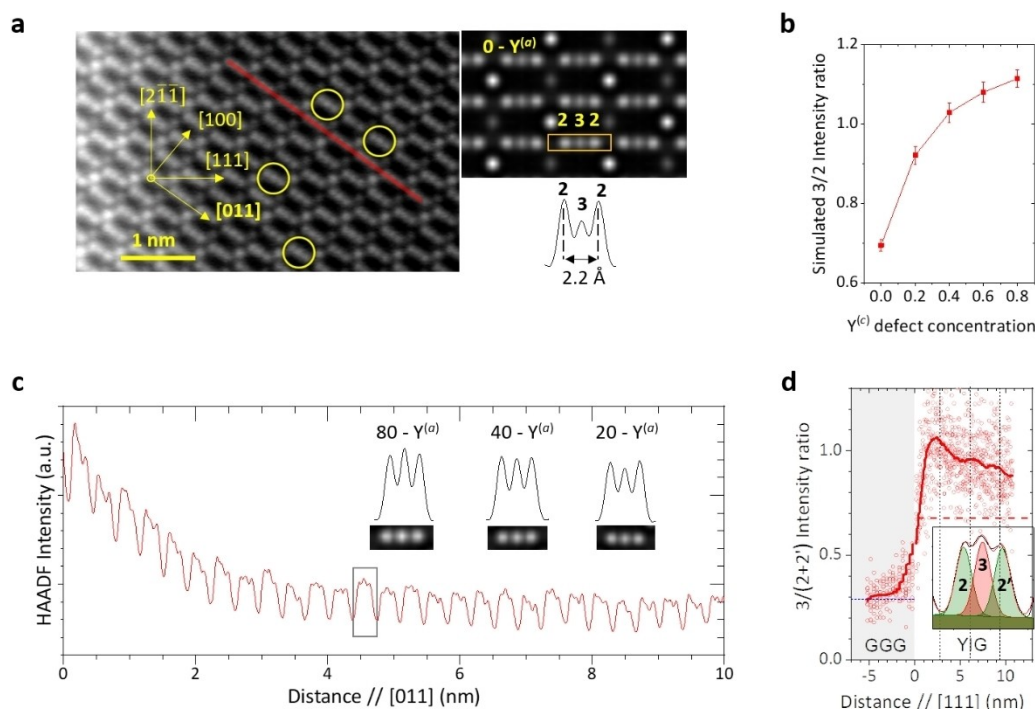
The second feature referred to above is that all concentration curves approximately intersect at a value of 10 at% (see Figure 3e), in agreement with the nominal total-cation versus oxygen ratio. This indicates that at the crossing point there is 5 at% excess of Y and Gd atoms relative to the number of available dodecahedral (*c*) sites. This interdiffusion unbalance across the interface should cause (*c*)-site cation excesses which, according to atomistic calculations on the energetics of cation disorder in garnets are expected to be accommodated through the formation of antisite defects.<sup>[36]</sup>

Figure 4a provides a closer look to the YIG/GGG interface. In this projection cationic columns draw a honeycomb-like pattern elongated along the [011] direction. As shown in the simulated image (right panel), the long sides of the hexagonal motif are formed by three closely located, 1.1 Å apart, cationic columns, labelled 2 or 3 depending on their composition and structure: Along column 2, dodecahedral Y<sup>(c)</sup> sites alternate with tetrahedral Fe<sup>(d)</sup> sites, while column 3 is composed by octahedral Fe<sup>(d)</sup> chains. The other two columns, alternating along rows with the 2-3-2 triplets, are formed by chains of dodecahedral Y<sup>(c)</sup> (bright) and tetrahedral Fe<sup>(d)</sup> (darker) coordination, respectively.

The theoretical image contrast clearly reflects the atomic number difference between different columns. Both 2 and 3-type columns have the same atomic density and therefore their HAADF intensities can be directly compared. Since the

average atomic number of column 2,  $\langle Z \rangle = 32.5$ , is larger than the Fe atomic number,  $Z = 26$ , the intensity of the central peak in each triplet should be lower than that of the neighboring ones. Careful inspection of the experimental image, however, reveals that in many triplets within the YIG film the central column is more intense than the side ones (examples are indicated by circles). In order to inquire into the origin of this contrast inversion, Figure 4b shows the calculated concentration dependence of the 3/2 intensity ratio (see also inset in Figure 4c). It can be readily seen that the introduction of Y<sup>(a)</sup> defects in the octahedral sublattice causes an apparent relative increase of the intensity of the central column (3). We note, however, that there are factors not taken into account in the simulation that might alter the image contrast and therefore an estimation of the antisite defect concentration: (i) the occurrence of Gd<sup>(a)</sup> antisite defects within the interdiffusion zone, which may lead to an overestimation of the actual concentration of Y<sup>(a)</sup> ones, (ii) local lattice distortions associated with the occurrence of the defects and, (iii) inhomogeneous distribution of the defects along the atomic columns.<sup>[49]</sup> Hence, this analysis is intended as a qualitative appraisal of the image contrast dependence on Y<sup>(a)</sup> concentration.

In order to estimate the strain associated to the observed population of Y<sup>(a)</sup> defects one needs to consider the misfit constraint imposed by the substrate. According to atomistic



**Figure 4.** a) High resolution HAADF image viewed along the [01-1] zone axis illustrating in detail the contrast in the vicinity of the YIG/GGG interface. Red line shows the path of the intensity profile shown in c). Right panel: Image simulation for stoichiometric YIG identifying different types of atomic columns with numbers, and corresponding HAADF intensity profile. The central column (3) has a lower intensity than neighboring 2-type columns according with its smaller average atomic number. Examples deviating from this rule are indicated by circles in the experimental image. b) Simulated 3/2 intensity ratio as a function of defect concentration. c) Experimental HAADF intensity profiles obtained through the 2-3-2 triplets along the [011] direction. The inset shows image simulations corresponding to increasing concentrations of Y<sup>(a)</sup> antisite defects, and corresponding intensity profiles. d) Variation of the 3/2 intensity ratio with distance from the substrate along the film normal, [111]. The solid line corresponds to a Savitzky-Golay type smoothing of the experimental data. Inset illustrates the fitting procedure.

calculations, inserting one  $Y^{(a)}$  excess defect per unit cell (8 f.u.) causes a 0.72% increase in volume.<sup>[23]</sup> This indicates that an Y excess as small as 0.62 at% increases the YIG lattice parameter from 12.376 Å to 12.406 Å, switching the misfit strain from tensile to compressive on GGG ( $a = 12.380$  Å). In our case, the occurrence of larger  $Gd^{(a)}$  defects in the interdiffusion region should induce even larger dilations. It appears that the observed uniaxial stretching does not only reflect the chemical expansion associated with the defects, but is further enhanced by the Poisson contribution. Using a Poisson ratio along the [111] direction of  $\nu_{[111]} = 0.29$ , one obtains an additional elongation of 0.0015 (see Figure S2). Therefore, one  $Y^{(a)}$  antisite defect per unit cell would account for a net stretching of 0.40%, which is more than half the 0.7% strain background measured by GPA in the bulk film. This shows that very low defect concentrations, even close or below the resolution limit of the EDS analysis, can induce significant strain levels.

We now analyze the spatial distribution of antisite defects in more detail. Figure 4d shows an experimental HAADF intensity profile through the 2–3–2 triplets (along the [011] direction). As can be seen, the relative intensity of the central peaks increases towards the substrate, before the background slope increases due to the increase in Gd concentration. It can also be observed that in the bulk film many triplets exhibit an asymmetric intensity distribution, which evidences unequal occupancies of the mixed side columns (denoted by 2 and 2', see inset in Figure 4d). The origin of this disorder is not straightforward due to possible competition of other defects, which according to their relative formation energies could be tetrahedral yttrium antisites ( $Y^{(d)}$ ), non-excess  $Y^{(a)}$  resulting from the disorder reaction  $Y^{(c)} + Fe^{(a)} \rightarrow Y^{(a)} + Fe^{(c)}$ , and tetrahedral vacancies<sup>[22–24]</sup>, although in agreement with the resulting intensity variations their contribution should be secondary compared with excess  $Y^{(a)}$  defects.

To obtain statistical trends, Figure 4d shows results from a large number of [011] atomic rows, where the solid curve corresponds to a Savitzky-Golay type smoothing of the

experimental data.<sup>[37]</sup> It can be observed that the transition from the substrate (shadowed area) to the film is characterized by an abrupt increase of the  $3/2$  ( $3/[(2+2')/2]$ ) intensity ratio, consistent with the concomitant compositional variation of the atomic columns, and reaches a first maximum within the Gd diffusion length which is thought to reflect the occurrence of  $Gd^{(a)}$  excess antisite defects. Beyond this maximum the intensity ratio decays drawing an oscillation similar to that observed in the normal strain profile (see Figure 2c), suggesting a possible fluctuation of the chemical expansion along the growth direction. At the second peak the intensity ratio adopts a value of 0.96 which, according to image simulations would correspond to an Y excess of 2.9 at%. We note that this value is in qualitative agreement with the local Y excess observed at this position in the EDS elemental profile (Figure 3e). The position of this second peak coincides with that of the second strain peak, arrowed in Figure 2c, in agreement with the accumulation of Y at the boundary of the Gd diffusion zone. Beyond this Y-enriched layer, the  $3/2$  intensity ratio is kept above the stoichiometric value indicating the persistence of a background concentration of  $Y^{(a)}$  defects in consistency with Y-excess fluctuations seen in EDS (Figure 3f), and the residual strain observed by GPA (see Figure 2).

In order to determine the saturation magnetization,  $M_s$ , and the Gilbert damping constant, we conducted frequency-dependent FMR measurements (see Figure S3). As argued by Gallagher *et al.* from a comparative study using various measuring approaches, this technique is particularly suited for the determination of  $M_s$  in thin films, where uncertainties may arise from the estimation of the film thickness, particularly in the presence of chemically diffused interfaces, and from the paramagnetic contribution of the GGG substrate.<sup>[12]</sup> Figure 5a shows the excitation frequency,  $f$ , as a function of the resonance field,  $H_r$ . From the fit of the experimental data using the Kittel formula,<sup>[38,39]</sup>  $f = \frac{\gamma}{2\pi} \sqrt{H_0(H_0 + 4\pi M_{eff})}$ , one obtains the reduced gyromagnetic ratio  $\gamma/2\pi = 2.850 (\pm 0.003)$  GHz/kOe and the effective magnetization  $4\pi M_{eff} = 2.18 (\pm 0.01)$  kOe. The magnet-

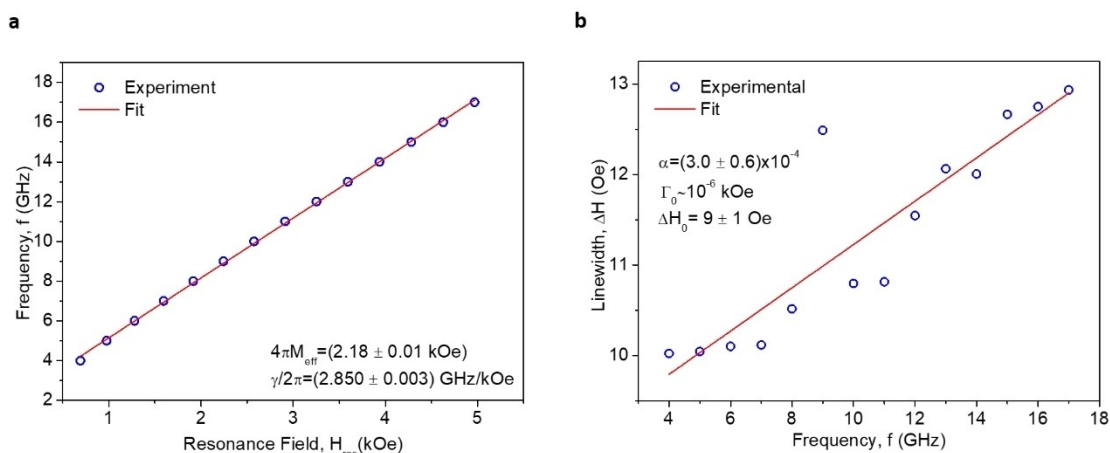


**Figure 5.** a) Ferromagnetic resonance frequency as a function of applied magnetic field. The blue circles represent the resonance field for a given frequency and the solid red line the Kittel fit. From the linear fit we extract the value of the gyromagnetic ratio ( $\gamma$ ) and the effective magnetization ( $4\pi M_{eff}$ ). b) Frequency dependence of FMR peak-to-peak linewidth. The open blue circles show the experimental data and the red solid line the fit according to Equation 2.

ization at saturation,  $M_s$ , is related to  $M_{eff}$  by  $4\pi M_{eff} = 4\pi M_s - H_{ani}$ , where  $H_{ani} = \frac{2|K_1|}{M_s} + \frac{4|K_2|}{M_s}$  is the anisotropy field. Using the first and second order anisotropy constants of YIG,  $K_1 = -6100$  erg/cm<sup>3</sup> and  $K_2 = -260$  erg/cm<sup>3</sup>,<sup>[43]</sup> one obtains  $4\pi M_s = 2.10 (\pm 0.01)$  kOe, about 20% larger than the bulk one, 1.73–1.75 kOe.<sup>[31]</sup> Similar high values have been reported for other YIG thin films grown on GGG by magnetron sputtering,  $4\pi M_s = 2.172$ – $2.141$  kOe,<sup>[12]</sup> and PLD,  $4\pi M_s = 2.100$  kOe.<sup>[41,42]</sup> Although, unfortunately, those reports do not address the defect chemistry of the films and, therefore, it is not possible to rationalize their magnetic behavior in terms of site-selective dilution effects, according to the present observations this increased value is in qualitative agreement with a selective suppression of the magnetic moment in the minority octahedral sublattice induced by the observed non-magnetic  $Y^{(a)}$  defects.

Interestingly, one finds in the literature that films exhibiting different magnetism also differ in the shape of their interdiffusion profiles. For instance, in contrast with our results, Mitra et al. report magnetization suppression in films exhibiting two crossing points, one at  $\approx 12$  at% for Fe/Ga and another at  $\approx 5$  at% for Gd/Y, indicating a strong deficiency in Y and Gd ions at the interface<sup>[11]</sup>. In strong contrast, Gallagher et al. report high magnetization, similar to that observed in the present work, in films also exhibiting a unique crossing point at  $\approx 10$  at%, and anomalous lattice stretching along the [111] direction<sup>[12]</sup>, reminiscent of the chemical expansion by  $Y^{(a)}$  defects observed in this work. This observation suggests, in fact, a strong impact of interdiffusion behavior on the magnetization of the films. Unbalanced interdiffusion results in stoichiometric deviations and the formation of antisite defects which may alter the ferrimagnetic balance among the different sublattices in different ways. Thus, most importantly, this behavior underlines a challenging need for precise control of interdiffusion in this complex system.

To precisely determine the Gilbert damping parameter,  $\alpha$ , the inhomogeneous linewidth broadening  $\Delta H_0$  and the strength of the two-magnon scattering,  $\Gamma_0$ , we fit the linewidth versus excitation frequency data using the following equation:

$$\Delta H = \Delta H_0 + \frac{8\pi\alpha f}{\sqrt{3}\gamma} + \Delta H_{TMS} \quad (1)$$

where the first term corresponds to the inhomogeneous broadening, and the second term is the intrinsic contribution to the linewidth which is proportional to the frequency with a slope determined by Gilbert damping parameter,  $\alpha$ . For a homogeneously in-plane magnetized thin film, the third term, corresponding to the TMS broadening, can be approximately expressed as,<sup>[43–45]</sup>

$$\Delta H_{TMS} = \frac{2}{\sqrt{3}} \Gamma_0 \sin^{-1} \left[ \frac{[f^2 + (f_0/2)^2] - f_0/2}{[f^2 + (f_0/2)^2] + f_0/2} \right]^{1/2} \quad (2)$$

where  $f_0 = (\gamma/2\pi)4\pi M_{eff}$ . When the orientation of the applied field (and the magnetization) is in-plane,  $\Gamma_0$  can be considered constant.<sup>[43]</sup> Figure 5b shows the FMR linewidth as a function of excitation frequency. The obtained damping parameter is  $\alpha =$

$3.0 \pm 0.6 \cdot 10^{-4}$ , which is comparable with the lowest values so far reported in the literature for PLD grown YIG/GGG nanometer-thick films.<sup>[15]</sup> Any increase in linewidth contributed by the TMS mechanism is a measure of the scattering rate of the uniform precession magnon into other spin-wave modes.<sup>[46]</sup> As can be observed in Figure 5b, the film under study exhibits a highly linear behavior of the linewidth and, accordingly, a very low value of the TMS strength,  $\Gamma_0 \approx 10^{-6}$  Oe, which reveals a highly ordered film, essentially free of defects or inhomogeneities that could act as scattering centers.

## Conclusion

These results highlight the ease of formation of  $Y^{(a)}$  antisite defects in nominally stoichiometric YIG films, particularly under conditions where unbalanced chemical interdiffusion across film-substrate interface favors the formation of excess Y ions relative to the number of dodecahedral (c) sites of the garnet structure. The occurrence of these defects is easily recognized through their chemical expansion, which under the constraint of the substrate results in an important lattice stretching along the [111] growth direction of 2.8% (rhombohedral distortion). More specifically, we observe a large concentration of Gd<sup>(a)</sup> and  $Y^{(a)}$  antisite defects within a ca. 4 nm thick interdiffusion zone, and accumulation of the latter in an adjacent  $\approx 2$  nm thick layer. Beyond this interfacial layer, the YIG still sustains a homogeneous stretching of 0.7% caused by a background concentration of  $Y^{(a)}$  antisite defects populating the entire film volume. Despite lattice distortions and cationic disorder, the film exhibits a high structural coherency, and FMR yields a low Gilbert damping parameter,  $\alpha = 3.0 \pm 0.4 \cdot 10^{-4}$ , and an almost negligible two-magnon scattering strength parameter,  $\Gamma_0 \approx 10^{-6}$  Oe. The saturation magnetization is higher than the bulk value, in consistency with the suppression of magnetic moment from the minority octahedral sublattice by replacement of Fe<sup>3+</sup> by nonmagnetic Y<sup>3+</sup>. In the light of these results, the recurrent observation of unexplained interfacial stretching by other authors strongly suggests that  $Y^{(a)}$  defects are a common feature in this system. These results emphasize a challenging need for control on interdiffusion to overcome the irreproducibility issue associated with thin YIG/GGG epitaxial films.

## Experimental Section

**Film growth:** Epitaxial Y<sub>3</sub>Fe<sub>5</sub>O<sub>12</sub> (yttrium iron garnet, YIG) films of about 25 nm thickness were deposited by PLD onto isostructural Gd<sub>3</sub>Ga<sub>5</sub>O<sub>12</sub> (GGG) single crystal substrates with (111) orientation (Crytec GmbH, roughness < 1 nm). The YIG target was prepared by conventional solid state reaction from Y<sub>2</sub>O<sub>3</sub> and Fe<sub>2</sub>O<sub>3</sub> powders (above 99.9% purity from Sigma Aldrich). The conditions for the growth were: KrF excimer UV laser ( $\lambda = 248$  nm), laser energy fluence about 4 J/cm<sup>2</sup>, 1 Hz pulse repetition rate, deposition temperature T = 750 °C, oxygen pressure  $pO_2 = 1.5$  mTorr, and target-to-substrate distance of about 45 mm. After growth films were cooled down under the same  $pO_2$  at a rate of 10 °C/min.

**X-ray diffraction:** High-resolution XRD measurements ( $2\theta/\omega$  scans and reciprocal space maps) were carried out using a Malvern-Panalytical X'Pert-PRO MRD system with a 4-angle goniometer, and using  $\text{Cu K}\alpha_1$  radiation ( $\lambda = 1.5406 \text{ \AA}$ , using a  $2\cdot\text{Ge}(220)$  monochromator).

**Ferromagnetic resonance:** Broadband FMR measurements were performed utilizing a NanOsc PhaseFMR spectrometer and  $200 \mu\text{m}$ -wide coplanar waveguide (CPW). The dc magnetic field  $H$ , generated by the electromagnet, is modulated using a time varying field produced by a Helmholtz coil,  $h_{ac}(t)$ , parallel to  $H$  with a frequency of  $490 \text{ Hz}$  and a field strength of  $1 \text{ Oe}$ . The YIG sample was placed face-down on the CPW and a RF microwave signal of frequency  $f$  is injected from the spectrometer, therefore producing a RF microwave field  $h_{rf}$  perpendicular to the modulated field  $H + h_{ac}(t)$ . The measurements were performed at room temperature, at a fixed frequency in the range from  $4 \text{ GHz}$  to  $17 \text{ GHz}$ , while sweeping the field through the resonance condition up to  $5 \text{ kOe}$ . To extract the resonance field and peak-to-peak linewidth at a specific frequency, each of the resonance spectra is fitted with the first derivative of an asymmetric Lorentzian function.

**X-ray absorption spectroscopy and X-ray magnetic circular dichroism:** XAS and XMCD measurements were carried out at the BOREAS beamline of the ALBA Synchrotron Light Source<sup>[47]</sup> in total electron yield (TEY) mode. Fe spectra were recorded across the  $L_{2,3}$  absorption edges. The XMCD spectrum was calculated from the difference between the XAS spectra for right ( $\sigma+$ ) and left ( $\sigma-$ ) almost 100% circularly polarized light. The XAS and XMCD measurements were performed at room temperature under an external magnetic field of  $2 \text{ Tesla (T)}$ , which was applied along the out-of-plane direction of the films (i.e., along the beam direction).

**Transmission electron microscopy:** Samples for transmission electron microscopy (TEM) were prepared by  $\text{Ga}^+$  Focused Ion Beam (FIB) milling using a FEI Helios 450 machine. Silicon oxide and tungsten layers were deposited to protect the regions of interest from the tails of the ion beam. A  $16 \text{ kV}$  operation voltage for the initial thinning was used and then a low beam energy in the range  $5\text{--}8 \text{ kV}$  to reduce FIB-induced damage. TEM experiments were performed on a probe-corrected ThermoFisher Scientific Titan Themis operated at a high voltage of  $200 \text{ kV}$ . High Angle Annular Dark Field (HAADF) images were acquired in Velox software for a multiframe acquisition allowing for an effective electron dose partitioning and a scan error free acquisition. The HAADF acquisition was done with a probe current of  $\sim 80 \text{ pA}$  and a dwell time of  $200 \text{ ns}$  corresponding to a dose of  $1.27\cdot 10^2 \text{ e}^-/\text{\AA}^2$  (considering a  $1 \text{ \AA}$  probe size). The incident convergence angle was set to  $\sim 20.7 \text{ mrad}$ , while inner and outer HAADF collection angles were equal to  $\sim 77.8 \text{ mrad}$  and  $\sim 230 \text{ mrad}$ , respectively. EDS and EELS spectra were collected in Gatan Microscopy Suite<sup>®</sup> (GMS) software. EDS spectra were acquired using the Super-X system that comprises four  $30 \text{ mm}^2$  windowless silicon drift detectors placed at an elevation angle of  $18^\circ$  from the horizontal with a symmetrical distribution along the beam axis ( $45^\circ$ ,  $135^\circ$ ,  $225^\circ$  and  $315^\circ$  azimuthal angles) and a  $0.64 (\pm 0.06)^\circ$  total solid angle. EDS mappings were obtained with the resolution of  $100\cdot 50$  pixels (pixel size of  $\sim 0.32 \text{ nm}$ ) using a dwell time of  $100 \text{ ms}$ . The quantification was performed using the k-factors implemented in GMS. As k-factors do not take into account the absorption and the specific orientation of the lamella with respect to the detectors, k-factors from  $\text{Fe}_2\text{O}_3$ ,  $\text{Ga}_2\text{O}_3$ ,  $\text{Gd}_2\text{O}_3$  and  $\text{Y}_2\text{O}_3$  were adjusted such as to match the composition far from the interface with the theoretical one. This method is validated from the derived oxygen content profile which fits very well the theoretical composition (k-factors are relative to the oxygen concentration and therefore the oxygen content cannot be adjusted). EELS spectra were acquired on a post-filter CCD US1000 camera mounted onto a GIF Quantum ER, with a

collection semi-angle of  $\sim 100 \text{ mrad}$ , a drift tube voltage of  $400 \text{ V}$  (in dual-EELS mode for zero-loss centering) and a dispersion of  $0.25 \text{ eV/pixel}$ . Hyperspectral mappings comprised of  $218\cdot 30$  pixels with a pixel size of  $\sim 0.2 \text{ nm}$  were acquired with a dwell time of  $0.1 \text{ ms}$  and  $100 \text{ ms}$  for the low-loss and high-loss regions, respectively. Using subpixel scanning, the above-mentioned acquisition parameters correspond to EDS and EELS dose-per-frame of  $9.75\cdot 10^2$  and  $1.91\cdot 10^3 \text{ e}^-/\text{\AA}^2$ . Note also that STEM images were acquired before and after any EDS or EELS acquisition to verify the overall structural integrity.

The intensity of the atomic columns in the HAADF image was analyzed extracting a number of separate linear scans (more than 30) parallel to the  $[011]$  crystallographic direction passing through the peak center of mass with a certain line width of several pixels (10) to integrate most of the column intensities. Each linear scan was then fitted to independent Gaussian functions for each atomic column to extract their position and intensity. For simplicity of the fitting process the Gaussian peaks were assumed to have a common width for all columns of the same type. Intensity ratios were measured for adjacent columns and plotted against their corresponding average positions along the growth direction. The data were averaged by applying a Savitzky-Golay type smoothing to a single line profile in a window of 200 points, and polynomials up to order two.

HAADF image simulations were performed using the quantum excitation of phonons model in  $\mu\text{STEM}$ .<sup>[48]</sup> A simple crystal model was prepared using the YIG unit cell projected along the  $[110]$  direction. Structural and thermal parameters were obtained from ref. [21]. Qualitative simulations were performed considering the employed HAADF-STEM imaging experimental conditions (alpha angle  $20 \text{ mrad}$ , collection angles: inner  $77 \text{ mrad}$  and outer  $230 \text{ mrad}$ , and foil thickness  $80 \text{ nm}$ ). The image contrast may be affected by the location and distribution of the antisites along the atomic columns.<sup>[49]</sup> Here, we considered a homogenous distribution of the Y-antisite defects along the Fe octahedral columns (column 3 in the text), namely, the antisites were introduced by fractionating the atom ( $n\text{Fe} + (1-n)\text{Y} = 1$ ) in the unit cell. The concentration of defects was simulated from 0 up to 80% in 20% steps.

## Acknowledgements

We thank Audrey Jannaud for FIB preparation of the TEM lamellae. We thank Prof. Dave McComb for discussions and access to Ohio Supercomputer Center. Part of this work was carried out through the access to HRTEM and XAS/XMCD facilities granted by the NFFA-Europe Infrastructure (proposals ID 678 and ID 571) under Horizon 2020 EU Funding Program. This work was supported in part by the Spanish Ministry of Economy, Industry and Competitiveness (project PID2019-108573GB-C21), and by the Catalan AGAUR agency (project: 2017-SGR-579). ICN2 is funded by the CERCA programme/ Generalitat de Catalunya and by the Severo Ochoa programme (SEV-2017-0706). ICMAB-CSIC is funded by the Severo Ochoa programme (CEX2019-000917-S). CG and JS acknowledge funding from the European Union's Horizon 2020 research and innovation program under the Marie Skłodowska-Curie grant agreement No. 101007825 (ULTIMATE-I Project). MV acknowledges funding by PID2020-116181RB-C32/MCIN/AEI/10.13039/501100011033. C.G. and C.R. acknowledge the financial support received by ANID FONDECYT/REGULAR 1201102. This



work was also supported by grant ANID PIA/APOYO AFB180002. F. S. acknowledges the Spanish Ministry of Industry, Economy and Competitiveness (project no. RTI2018-098537-B-C21).

## Conflict of Interest

The authors declare no conflict of interest.

## Data Availability Statement

The data that support the findings of this study are available from the corresponding author upon reasonable request.

**Keywords:** yttrium iron garnet · thin film · antisite defects · Gilbert damping · magnetization

- [1] E. J. J. Mallmann, A. S. B. Sombra, J. C. Goes, P. B. A. Fecine, *Solid State Phenom.* **2013**, *202*, 65–96.
- [2] J. Douglas Adam, L. E. Davis, G. F. Dionne, E. F. Schloemann, S. N. Stitzer, *IEEE Trans. Microwave Theory Tech.* **2002**, *50*, 721–737.
- [3] B. J. H. Stadler, T. Mizumoto, *IEEE Photon. J.* **2014**, *6*, 0600215.
- [4] A. A. Serga, A. V. Chumak, B. Hillebrands, *J. Phys. D* **2010**, *43*, 264002.
- [5] H. Yu, O. d'Allivy Kelly, V. Cros, R. Bernard, P. Bortolotti, A. Anane, F. Brandl, R. Huber, I. Stasinopoulos, D. Grundler, *Sci. Rep.* **2014**, *4*, 6848.
- [6] V. V. Kruglyak, S. O. Demokritov, D. Grundler, *J. Phys. D* **2010**, *43*, 264001.
- [7] S. M. Rezende, R. L. Rodríguez-Suárez, M. M. Soares, L. H. Vilela-Leão, D. Ley Domínguez, A. Azevedo, *Appl. Phys. Lett.* **2013**, *102*, 1–4.
- [8] M. B. Jungfleisch, V. Lauer, R. Neb, V. Chumak, B. Hillebrands, *Appl. Phys. Lett.* **2013**, *103*, 2011–2015.
- [9] Y. Sun, H. Chang, M. Kabatek, Y.-Y. Song, Z. Wang, M. Jantz, W. Schneider, M. Wu, E. Montoya, B. Kardasz, B. Heinrich, S. G. E. Te Velthuis, H. Schultheiss, A. Hoffmann, *Phys. Rev. Lett.* **2013**, *111*, 106601.
- [10] C. Dubs, O. Surzhenko, R. Thomas, J. Osten, T. Schneider, K. Lenz, J. Grenzer, R. Hübner, E. Wendler, *Phys. Rev. Mater.* **2020**, *4*, 024416.
- [11] A. Mitra, O. Cespedes, Q. Ramasse, M. Ali, S. Marmion, M. Ward, R. M. D. Brydson, C. J. Kinane, J. F. K. Cooper, S. Langridge, B. J. Hickey, *Sci. Rep.* **2017**, *7*, 11774.
- [12] J. C. Gallagher, A. S. Yang, J. T. Brangham, B. D. Esser, S. P. White, M. R. Page, K. Y. Meng, S. Yu, R. Adur, W. Ruane, S. R. Dunsiger, D. W. McComb, F. Yang, P. C. Hammel, *Appl. Phys. Lett.* **2016**, *109*, 072401.
- [13] S. A. Manuilov, S. I. Khartsev, A. M. Grishin, *J. Appl. Phys.* **2009**, *106*, 123917.
- [14] S. A. Manuilov, A. M. Grishin, *J. Appl. Phys.* **2010**, *108*, 013902.
- [15] C. Hauser, T. Richter, N. Homonnay, C. Eismenschmidt, M. Qaid, H. Deniz, D. Hesse, M. Sawicki, S. G. Ebbinghaus, G. Schmidt, *Sci. Rep.* **2016**, *6*, 20827.
- [16] S. M. Sutorin, A. M. Korovin, V. E. Bursian, L. V. Lutsev, V. Bourobina, N. L. Yakovlev, M. Montecchi, L. Pasquali, V. Ukleev, A. Vorobiev, A. Devishvili, N. S. Sokolov, *Phys. Rev. Mater.* **2018**, *2*, 104404.
- [17] I. Lucas, P. Jiménez-Cavero, J. M. Vila-Funqueiriño, C. Magén, S. Sangiao, J. M. deTeresa, L. Morellón, F. Rivadulla, *Phys. Rev. Mater.* **2017**, *1*, 074407.
- [18] J. M. Gomez-Perez, S. Vélez, L. McKenzie-Sell, M. Amado, J. Herrero-Martín, J. López-López, S. Blanco-Canosa, L. E. Hueso, A. Chuvilín, J. W. A. Robinson, F. Casanova, *Phys. Rev. Appl.* **2018**, *10*, 044046.
- [19] B. B. Krichevstov, S. V. Gastev, S. M. Sutorin, V. V. Fedorov, A. M. Korovin, V. E. Bursian, A. G. Banskchikov, M. P. Volkov, M. Tabuchi, N. S. Sokolov, *Sci. Technol. Adv. Mater.* **2017**, *18*, 351–363.
- [20] N. S. Sokolov, V. V. Fedorov, A. M. Korovin, S. M. Sutorin, D. A. Baranov, S. V. Gastev, B. B. Krichevstov, K. Y. Maksimova, A. I. Grunin, V. E. Bursian, L. V. Lutsev, M. Tabuchi, *J. Appl. Phys.* **2016**, *119*, 023903.
- [21] S. Geller, M. A. Gilleo, *J. Phys. Chem. Solids.* **1957**, *3*, 30–36.
- [22] S. Tan, W. Zhang, L. Yang, J. Chen, Z. Wang, *J. Appl. Phys.* **2020**, *128*, 183904.
- [23] T. Su, S. Ning, E. Cho, C. A. Ross, *Phys. Rev. Mater.* **2021**, *5*, 094403.
- [24] H. Donnerberg, C. R. A. Catlow, *J. Phys.: Condens. Matter* **1993**, *5*, 2947–2060.
- [25] P. Novák, J. Englich, H. Stepánková, J. Kohout, H. Lütgemeier, K. Wagner, W. Tolksdorf, *J. Phys. IV France Colloque C1* **1997**, *7*, 283–286.
- [26] V. Chlan, H. Štěpánková, V. Procházka, J. Engliča, J. Kohouta, D. Nižňanský, J. Buršík, *J. of Magn. Magn. Mat.* **2005**, *290–291*, 993–996.
- [27] M. Kučera, K. Nitsch, H. Štěpánková, M. Maryško, P. Reiche, *phys. stat. sol.* **2003**, *198*, 407–414.
- [28] W. Noun, E. Popova, F. Bardelli, Y. Dumont, R. Bertacco, A. Tagliaferri, M. Tessier, M. Guyot, B. Berini, N. Keller, *Phys. Rev. B* **2010**, *81*, 054411.
- [29] Y. Dumont, N. Keller, E. Popova, D. S. Schmool, M. Tessier, S. Bhattacharya, B. Stahl, R. M. C. Da Silva, M. Guyot, *Phys. Rev. B* **2007**, *76*, 104413.
- [30] G. Winkler, *Magnetic Garnets. Vieweg Tracts in Pure and Applied Physics*, Vol. 5. Springer-Verlag, Braunschweig/Wiesbaden, **1981**.
- [31] B. Lax, K. J. Button, *Microwave ferrites and ferrimagnetics*. Lincoln Laboratory publications, McGraw-Hill, New York, **1962**.
- [32] R. D. Shannon, *Acta Crystallogr. Sect. A* **1976**, *32*, 751–767.
- [33] S. J. Pennycook, D. E. Jesson, *Phys. Rev. Lett.* **1990**, *64*, 938–9041.
- [34] M. J. Hÿtch, *Microsc. Microanal. Microstruct.* **1997**, *8*, 41–57.
- [35] M. Liu, L. Jin, J. Zhang, Q. Yang, H. Zhang, P. Gao, D. Yu, *AIP Adv.* **2018**, *8*, 085117.
- [36] Ch. Milanese, V. Buscaglia, F. Maglia, U. Anselmi-Tamburini, *Chem. Mater.* **2004**, *16*, 1232–1239.
- [37] A. Savitzky, M. J. E. Golay, *Anal. Chem.* **1964**, *36*, 1627–1639.
- [38] C. Kittel, *Phys. Rev.* **1948**, *73*, 155–161.
- [39] S. S. Kalarickal, P. Krivosik, M. Wu, C. E. Patton, M. L. Schneider, P. Kabos, T. J. Silva, J. P. Nibarger, *J. Appl. Phys.* **2006**, *99*, 093909.
- [40] Y. Sun, M. Wu, in *Recent Advances in Magnetic Insulators – From Spintronics to Microwave Applications*, Vol. 64, (Eds: M. Wu, A. Hoffmann) Solid State Physics, Academic Press **2013**.
- [41] O. d'Allivy Kelly, A. Anane, R. Bernard, J. Ben Youssef, C. Hahn, A. H. Molpeceres, C. Carrétéro, E. Jacquet, C. Deranlot, P. Bortolotti, R. Lebourgeois, J.-C. Mage, G. de Loubens, O. Klein, V. Cros, A. Fert, *Appl. Phys. Lett.* **2013**, *103*, 082408.
- [42] C. Hahn, V. V. Naletov, G. de Loubens, O. Klein, O. d'Allivy Kelly, A. Anane, R. Bernard, E. Jacquet, P. Bortolotti, V. Cros, J. L. Prieto, M. Muñoz, *Appl. Phys. Lett.* **2014**, *104*, 152410.
- [43] J. Lindner, I. Barsukov, C. Raeder, C. Hassel, O. Posth, R. Meckenstock, P. Landeros, D. L. Mills, *Phys. Rev. B* **2009**, *80*, 224421.
- [44] K. Lenz, H. Wende, W. Kuch, K. Baberschke, K. Nagy, A. Jánossy, *Phys. Rev. B* **2006**, *73*, 144424.
- [45] R. Arias, D. L. Mills, *Phys. Rev. B* **1999**, *60*, 7395–7409.
- [46] A. Conca, S. Keller, M. R. Schweizer, E. T. Papaioannou, B. Hillebrands, *Phys. Rev. B* **2018**, *98*, 214439.
- [47] A. Barla, J. Nicolas, D. Cocco, S. M. Valvidares, J. Herrero-Martín, P. Gargiani, J. Moldes, C. Ruget, E. Pellegrin, S. Ferrer, *J. Synchrotron Radiat.* **2016**, *23*, 1507–1517.
- [48] L. J. Allen, A. J. D'Alfonso, S. D. Findlay, *Ultramicroscopy* **2015**, *151*, 11–22.
- [49] B. D. Esser, A. J. Hauser, R. E. A. Williams, L. J. Allen, P. M. Woodward, F. Y. Yang, D. W. McComb, *Phys. Rev. Lett.* **2016**, *117*, 176101.

Manuscript received: November 3, 2022  
Revised manuscript received: December 7, 2022  
Accepted manuscript online: December 9, 2022  
Version of record online: December 19, 2022